NRL Report 7782.

Bottom Reflectivity Experiments in the Deep Ocean Over Rugged Bottom Terrain

A. Zed Robinson, Jr., Lynn B. Poché, Jr., and Gerald A. Sabin

Methods and Systems Branch
Underwater Sound Reference Division

25 June 1974

NAVAL RESEARCH LABORATORY
Underwater Sound Reference Division
P.O. Box 8337, Orlando, Fla. 32806

SECURITY CLASSIFICATION OF THIS PAGE *(When Data Entered)*

REPORT DOCUMENTATION PAGE		READ INSTRUCTIONS BEFORE COMPLETING FORM
1. REPORT NUMBER NRL Report 7782	2. GOVT ACCESSION NO.	3. RECIPIENT'S CATALOG NUMBER
4. TITLE *(and Subtitle)* BOTTOM REFLECTIVITY EXPERIMENTS IN THE DEEP OCEAN OVER RUGGED BOTTOM TERRAIN		5. TYPE OF REPORT & PERIOD COVERED Final report on a part of the problem
		6. PERFORMING ORG. REPORT NUMBER
7. AUTHOR(*) A. Zed Robinson, Jr. Lynn B. Poché, Jr. Gerald A. Sabin		8. CONTRACT OR GRANT NUMBER(*)
9. PERFORMING ORGANIZATION NAME AND ADDRESS Naval Research Laboratory Underwater Sound Reference Division P. O. Box 8337, Orlando, Fla. 32806		10. PROGRAM ELEMENT, PROJECT, TASK AREA & WORK UNIT NUMBERS NRL Problem S02-30 Project No. RF 11-121-403
11. CONTROLLING OFFICE NAME AND ADDRESS Department of the Navy Office of Naval Research Arlington, Va. 22217		12. REPORT DATE 25 June 1974
		13. NUMBER OF PAGES iv + 42
14. MONITORING AGENCY NAME & ADDRESS*(if different from Controlling Office)*		15. SECURITY CLASS. *(of this report)* UNCLASSIFIED
		15a. DECLASSIFICATION/DOWNGRADING SCHEDULE

16. DISTRIBUTION STATEMENT *(of this Report)*

Approved for public release; distribution unlimited

17. DISTRIBUTION STATEMENT *(of the abstract entered in Block 20, if different from Report)*

18. SUPPLEMENTARY NOTES

19. KEY WORDS *(Continue on reverse side if necessary and identify by block number)*

Ocean bottom reflectivity
Deep ocean
Energy spectral density
Computer data reduction

Fast Fourier transform
Ocean bottom sediment

20. ABSTRACT *(Continue on reverse side if necessary and identify by block number)*

In bottom-reflectivity experiments conducted in the Atlantic Ocean during September and October 1971, ½-lb blocks of TNT were used as the acoustic source. Data were collected from a hydrophone suspended 500 ft off the ocean floor. The experiments were designed so that direct and reflected signals incident on the suspended hydrophone could be separated in time. Recorded data were digitized, and energy spectral densities of the direct and the reflected signals then were computed separately by fast Fourier transform (FFT) techniques and plotted on

DD FORM 1473 1 JAN 73   EDITION OF 1 NOV 65 IS OBSOLETE
S/N 0102-014-6601 |

i

20. Abstract (continued)

the same linear scale to show the bottom-reflection effects as a function of frequency. The experimental procedures are critically examined to expose their inadequacies and to provide information to future experimenters.

Contents

Foreword

Although the Underwater Sound Reference Division fully supports the use of metric (SI) units of measurement, particularly in underwater sound, British units have been retained in some sections of this report because these units actually were used during the experiments and the data were acquired in them. It was felt that conversion of these units to SI equivalents would detract from the report, but this fact should not be construed in any manner as an abandonment of the belief that orderly conversion to the International System of Units (SI) is essential to the underwater acoustics community.

BOTTOM-REFLECTIVITY EXPERIMENTS IN THE DEEP OCEAN OVER RUGGED BOTTOM TERRAIN

Introduction

The effect of a complex ocean bottom on the propagation of acoustic energy is one of the fundamental problems associated with ocean acoustics, particularly long-range propagation when the acoustic signal interacts strongly with the ocean bottom. The problem is summarized by Berman and Guthrie [1] and by Williams [2] in two papers that are part of a series that reviews the past twenty years in underwater acoustics.

In an idealized two-layer model, reflection from a smooth plane interface will follow the Rayleigh law, which may be expressed as

$$R = \frac{\rho_b c_b \sin \phi - \rho_0 (c_0^2 - c_b^2 \cos^2 \phi)^{\frac{1}{2}}}{\rho_b c_b \sin \phi + \rho_0 (c_0^2 - c_b^2 \cos^2 \phi)^{\frac{1}{2}}}, \tag{1}$$

where ρ_b is the density of the bottom, ρ_0 is water density, c_b is the sound speed in the bottom (complex where losses in the bottom exist), c_0 is the sound speed in the water, ϕ is the grazing angle, and R is the reflection coefficient for a plane wave originating in the water and reflected from the idealized bottom. An inspection of Eq. (1) shows that for c_0 greater than c_b (and no attenuation in the bottom), an angle of intromission is defined by

$$\rho_b c_b \sin \phi = \rho_0 (c_0^2 - c_b^2 \cos^2 \phi)^{\frac{1}{2}}, \tag{2}$$

where the reflection coefficient is zero and all acoustic energy is transmitted into the bottom. An abrupt 180-deg phase reversal in the reflection coefficient occurs at this angle of intromission; that is, for grazing angles larger than the angle of intromission, the reflection coefficient is positive, and for smaller grazing angles, it is negative. If the bottom introduces attenuation, the same effects are observed except that the angle of intromission is not as sharply defined; there is no absolute null in the reflection coefficient and the phase transition is gradual.

For calculation purposes, it is convenient to rewrite Eq. (1) in the form

$$R = \frac{\rho c \sin \phi - (1 - c^2 \cos^2 \phi)^{\frac{1}{2}}}{\rho c \sin \phi + (1 - c^2 \cos^2 \phi)^{\frac{1}{2}}}, \tag{3}$$

where $\rho = \rho_b/\rho_0$ is the normalized bottom sediment density, $c = (c_b/c_0) + j\gamma$ is the normalized sound speed in the bottom, and c_b is the real part of the sound speed in the bottom. The imaginary part of c represents the effect of attenuation in the bottom. For example, if $g(t - x/c)$ represents a traveling plane wave in the bottom, then the Fourier transform of $g(t - x/c)$ is given by $F_g(f)e^{-j\omega x/c}$. The sound speed in the bottom is given by $c_b + j\gamma c_0$. Now, for $c_b \gg \gamma c_0$,

$$\frac{1}{c_b + j\gamma c_0} \simeq \frac{1}{c_b} - j\frac{\gamma c_0}{c_b^2}.$$

The Fourier transform of $g(t - x/c)$ then becomes

$$[\exp(-\gamma \omega x c_0/c_b^2)]F_g(f)[\exp(-j\omega x/c_b)].$$

The factor $\exp(-\gamma \omega x c_0/c_b^2)$ expresses the attenuation over a path length of x units. The attenuation per unit length expressed in decibels is $20(\gamma \omega c_0/c_b^2)\log_{10}e$. If this attenuation per unit length is linearly dependent on frequency, then γ is a constant independent of frequency and the reflection coefficient is independent of frequency. Hamilton [3] reports such linear frequency dependence of attenuation in marine sediments. His equation for the attenuation is given by

$$\alpha = kf^n, \tag{4}$$

where α is in decibels per meter and f is in kilohertz, and where the reported values of n are all very close to unity with the constant k defining the attenuation characteristics. The γ of Eq. (3) is related to k in the following manner:

$$\gamma = 1.832(c_b/c_0)^2 c_0 k(10^{-5}), \tag{5}$$

where c_0 is in meters per second. A typical value of k for a clayey-silt bottom is 0.18. For sound speeds of about 1500 m/s, the corresponding value of γ is 0.005. Figure 1 is a plot of the reflection coefficient

as calculated from Eq. (3) with $\rho = 1.3$, $c_b/c_0 = 0.98$, and $\gamma = 0.005$. This figure illustrates the angle of intromission that occurs for values of c_0 greater than c_b.
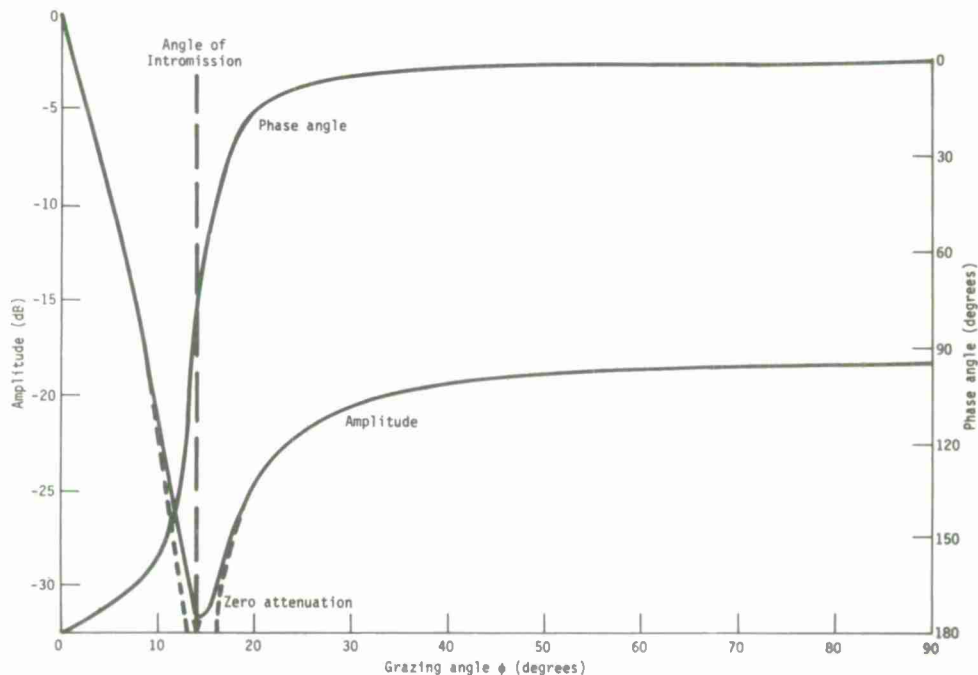

Fig. 1. Bottom reflection coefficient for c_0 greater than c_b, as calculated from Eq. (3) with $\rho = 1.3$, $c_b/c_0 = 0.98$, and $\gamma = 0.005$.

From Eq. (1) for the case where c_0 is smaller than c_b (and assuming zero attenuation), a critical angle is defined by

$$c_0^{\ 2} = c_b^{\ 2}\ \cos^2\phi. \tag{6}$$

At grazing angles smaller than the critical angle, there is complete reflection from the ocean bottom. There is zero phase shift in the reflection coefficient for grazing angles larger than the critical angle. There is gradual transition from 0 to 180 deg as the grazing angle is decreased below the critical angle to zero. The effect of attenuation in the bottom tends to keep the reflection coefficient from going completely to unity at the critical angle and causes a very small phase shift at grazing angles greater than the critical angle. Figure 2 is a plot of the reflection coefficient and its corresponding phase angle as a function of grazing angle for the values $\rho = 1.3$, $c_b/c_0 = 1.05$, and $\gamma = 0.005$. This figure illustrates the critical angle that occurs for values of c_b greater than c_0.
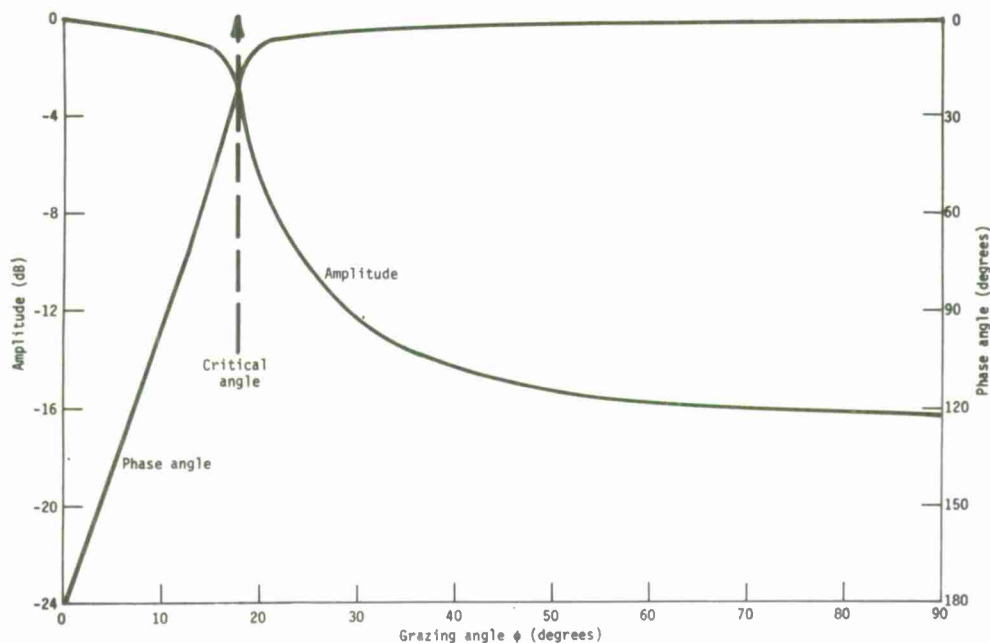
Fig. 2. Bottom-reflection coefficient for c_b greater than c_0, as calculated from Eq. (3) with $\rho = 1.3$, $c_b/c_0 = 1.05$, and $\gamma = 0.005$.

Although Rayleigh-like reflections have been observed in many instances, generally the idealized two-layer model has not been satisfactory. Expressions derived by Tolstoy and Clay [4] for a multilayered model give a more accurate description of the ocean bottom. In their model, it is assumed that a thin uniform sediment layer overlies a liquid medium of higher acoustic impedance. The multilayer model is a considerable improvement over the two-layer model, but it still does not provide an adequate description except for special cases. The principal difficulties with this model are:

1. Neither the sediment nor the ocean subbottom is completely homogeneous (that is, scattering generally occurs in all layers postulated). In addition, the incident signal can excite surface waves along the water-sediment interface.

2. The layer interfaces are not plane parallel surfaces. As a matter of fact, one would expect varying scales of roughness for the water-sediment interface and other subbottom interfaces. That is, in an area where the subbottom terrain is extremely rugged, one might expect the sediment formation to tend to smooth out the ruggedness of the bottom terrain.

3. In experiments involving localized bottom reflectivity, incident energy is not in the form of plane waves. Expanding the experimental geometry so as to approach plane wave conditions tends to defeat the concept of localized measurements.

4

4. Refractive effects in the water (and other layers) produced by sound speed gradients further complicate the problem. For example, the constant gradient that occurs in the deep ocean will have a nonnegligible effect on the grazing angle and on the divergence of the bottom-reflected signal. Calculations of these effects are given in Appendix A.

For these reasons, there is complete agreement with Williams [2] that experimentation and theory in regard to the ocean bottom effects must go hand in hand. We believe, however, that ultimately the effects of the bottom on propagation will have to be expressed in statistical terms to a far greater extent than in deterministic ones. That is, an average value for the propagation loss will be determined and a time-varying fade of the signal of a specified statistical character will be introduced. The implication of this kind of model is that signal receivers should be optimized on the basis of a fading signal.

For the various reasons stated above, it was decided to implement localized bottom-reflectivity experiments in a recent propagation-loss experiment in the Atlantic where the local bottom terrain was extremely rugged. This report will describe the bottom-reflectivity experiments and the data reduction. Particular emphasis will be placed on the potential of the experimental and data-reduction procedures, and on the exposed inadequacies of the original experiments and their implementation. Guidelines for improved experimental design will be proposed.

General Description of the Experiments

The basic experiments involved were patterned after those of Hastrup [5] in that explosive charges were used as signal sources, the experiments were designed so that temporal separation of the direct and reflected signals could be achieved, and processing techniques similar to Hastrup's were to be used. There were two basic experiments. Both consisted of recording acoustic signals from explosive charges as received by a hydrophone suspended a nominal 500 ft off the deep ocean floor. The signals received by the suspended hydrophone were transmitted back to the receiving ship by a multiplex FM telemetry system, with a coaxial cable as a hardwire telemetry link. The coaxial cable was an integral part of the anchoring cable. The telemetry signals were demodulated on board the receiving ship and recorded on magnetic tape by standard IRIG FM recording at 1-7/8 in./s. A 300-Hz low-pass filter was used at the output of each of the telemetry demodulators. Figure 3 illustrates the receiving ship and hydrophone configuration. Figure 4 is a block diagram of the electronic system used for data acquisition.

The first experiment consisted of detonating $\frac{1}{2}$-lb charges (with pressure-actuated detonators) at depths ranging from 4000 to 11,000 ft (in 1000-ft steps) at a fixed horizontal range from the receiving hydrophone (0.8 to 2.5 nautical miles, depending on the anchor scope of the receiving ship). The desired spread in the grazing angle was to be achieved by the variations in shot depth. The most serious problem expected with this experiment was the small energy likely to be available
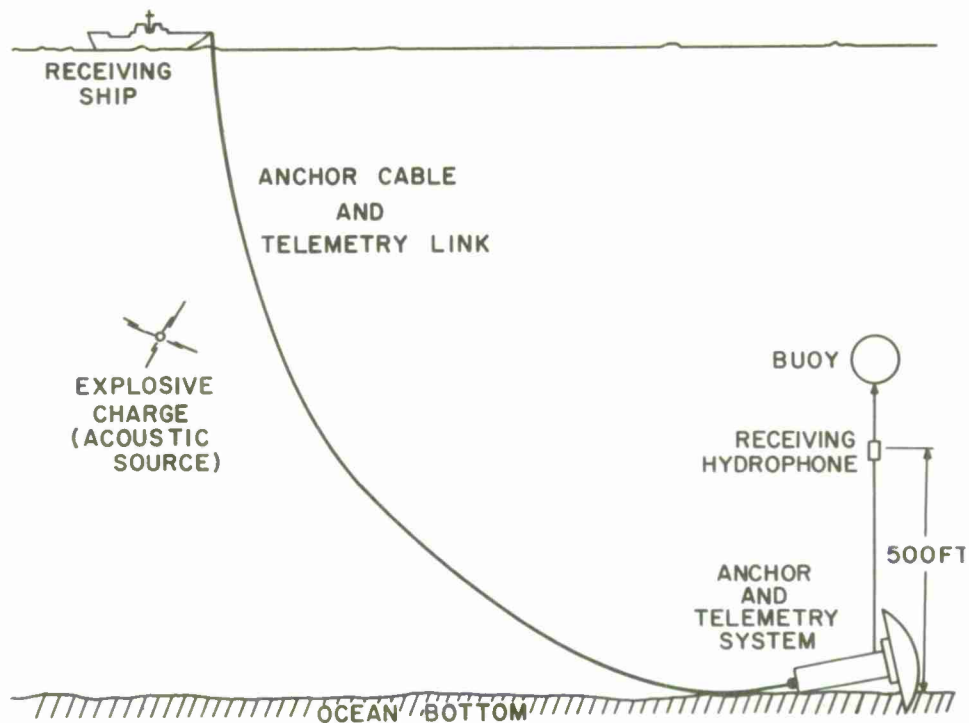
Fig. 3. Receiving ship and anchor-hydrophone configuration.
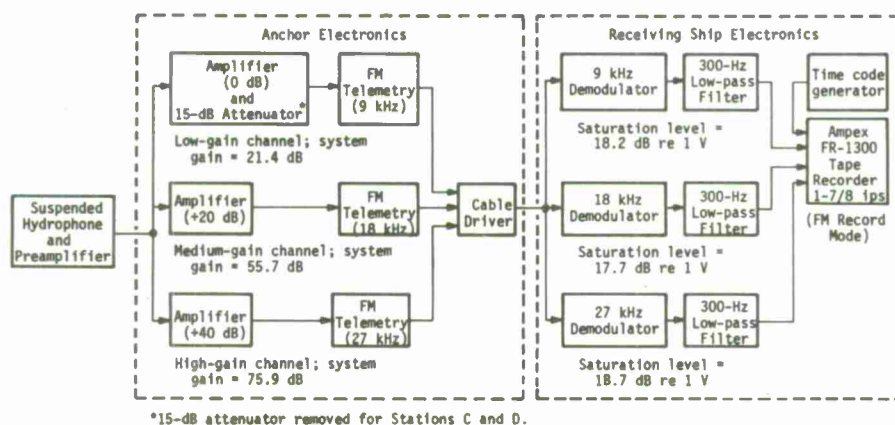
Fig. 4. Block diagram of anchor and receiving ship electronics.

6

from the deeper charges at frequencies below 200 Hz. A reduction in acoustic energy at the lower frequencies is to be expected at the greater depths because of an increased bubble oscillation frequency and a decreased bubble size.

The second experiment consisted of detonating ½-lb charges just below the surface so that the gas bubble vented on its initial expansion. Changes in horizontal separation between the charge and the receiving hydrophone that had to be made to provide the desired range in the grazing angle were produced by having a second ship deploy the charges at ½-mile intervals as she traversed a straight course directly over the receiving hydrophone.

Data Acquisition

Data were acquired at four different sites designated Stations A, B, C, and D. Figure 5 shows the area bathymetry at Station A, the anchor site, and the nominal geometry of the shots detonated. One sequence of
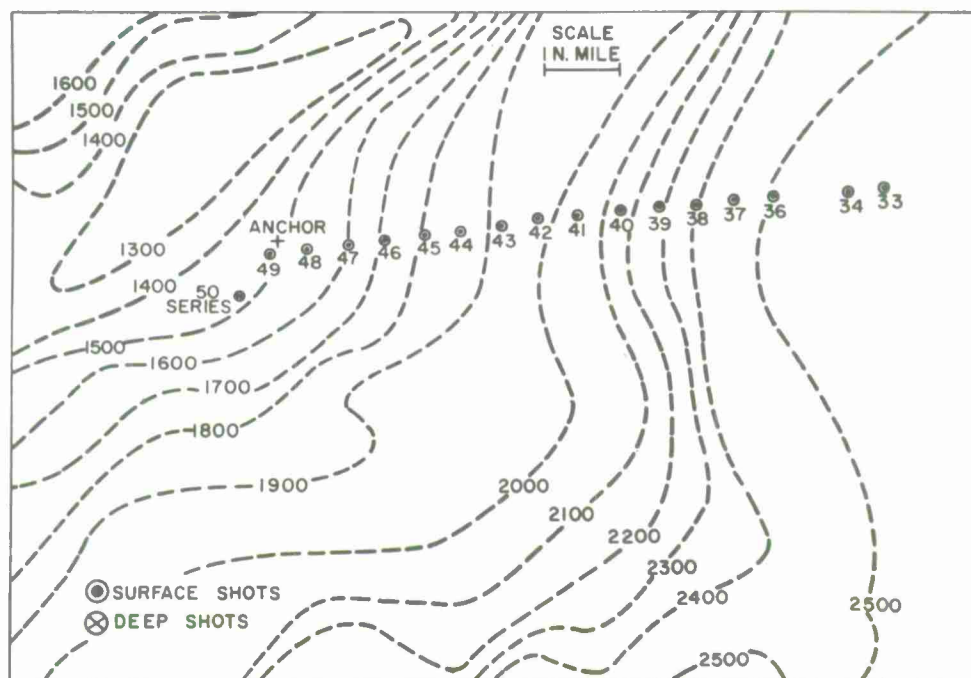
Fig. 5. Bathymetry and bottom-reflectivity shot geometry at Station A. Isobaths in fathoms.

eight deep shots (designated Series 50) was detonated at this station at depths ranging from 4000 ft through 7000 ft. Limited amounts of data were taken here because the weather was so calm that anchor scope was not adequate to give the desired range of grazing angles with charges dropped from the receiving ship. In retrospect, more data should have been taken, including charges detonated at 8000 ft. One sequence of sur-face charges (designated Series 30) was recorded at Station A as shown on Fig. 5. Because of the constant sound speed gradient in the deep ocean, no direct arrivals at the suspended hydrophones were observed for ranges greater than 10 nautical miles. This was true for all of the ex-periments with surface charges.

Fig. 6. Bathymetry and bottom-reflectivity shot geometry at Station B. Isobaths in fathoms.

Figure 6 shows the area bathymetry at Station B, the anchor site, and the nominal shot geometry. One sequence of eight deep charges (designated Series 100) was detonated at the receiving ship. Again, because of extremely calm weather, the desired anchor scope could not be achieved by the receiving ship. For this reason, a motorized raft was dispatched from the ship downslope of the anchor and two more sequences of deep charges (designated Series 200 and 300) were detonated and recorded. Each sequence contained 18 shots ranging in depth from 4000 ft through 9000 ft. One sequence of surface charges (designated Series 350) also was recorded at Station B.

Figure 7 shows the bathymetry at Station C, the anchor site, and the nominal geometry of the shots detonated. Two sequences of deep shots (desi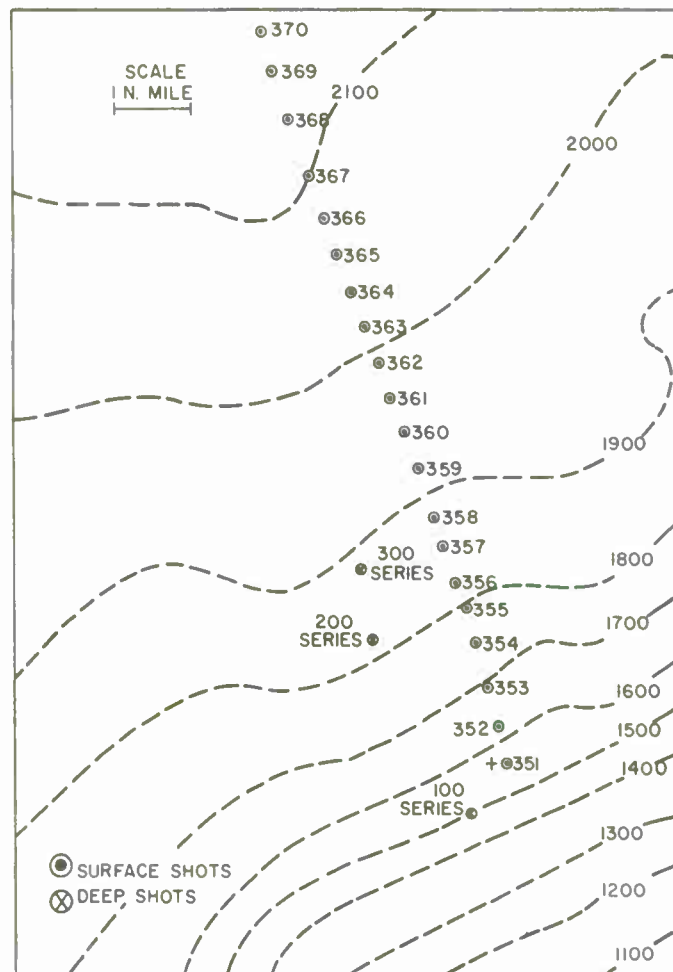gnated Series 500 and 600) were detonated and recorded at this station. Each sequence contained 15 shots ranging in depth from 4000 ft through 9000 ft. One sequence of surface charges (designated Series 900) also was recorded at this station. Before the experiments were conducted at Station C, a 15-dB attenuator pad was removed from the low-gain channel in the anchor electronics, which substantially increased the recorded signal-to-noise ratio, resulting in much improved data.
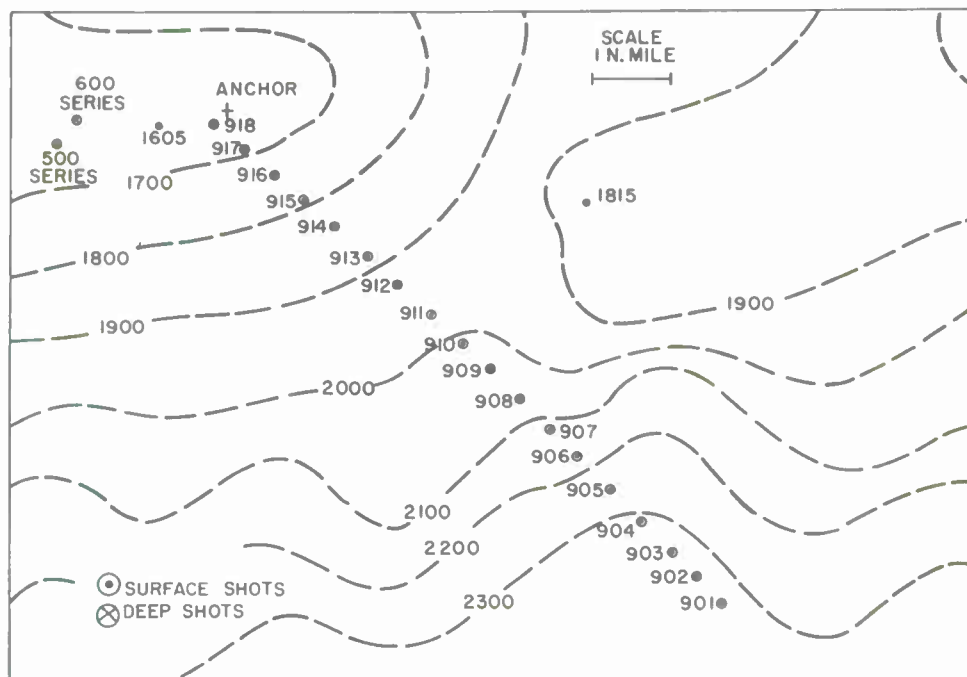

Fig. 7. Bathymetry and bottom reflectivity shot geometry at Station C. Isobaths in fathoms.

No bathymetry is shown for Station D because of the limited amount of data recorded there and because no information was logged on the position of the shot drops relative to the anchor. The anchor was positioned on a slope of approximately 10 deg. One sequence of twelve deep shots (designated Series 700) ranging in depth from 4000 ft through 8000 ft was detonated and recorded. No surface charges were recorded at this station.

In addition to the tape recordings made at each station, a log of ancillary information was maintained to allow for efficient data reduction and interpretation of results. Blasting caps were fired at the surface immediately after the anchor touched bottom at each station to give a measure of the actual height of the suspended hydrophone above the bottom. This height was 500 ft for Stations A, C, and D, and 475 ft for Station B. Most of the information so logged is not included in this report because it is not pertinent to the reduced data.

Data Reduction

The experimental design concept was based on the generation of a signal of sufficiently short duration that the direct signal and the reflected signal could be separated in time at the suspended hydrophone. This time separation allowed separate processing of the direct and the reflected signals. The data examined initially were from the deep-shot experiments. Several methods of data reduction were investigated, but it became obvious that the superior method would involve translation of the magnetic tape analog signals to a digital format so that the USRD's PDP-8/I computer could be used. It was obvious also that the early data were contaminated by low-frequency noise radiated from the receiving ship that at times contained a discrete component of approximately 15 to 20 Hz.

The data-reduction process used was as follows.

1. The analog tapes were played back at the tape speed 7½-in./s (or at four times the recording speed). The recorded output was passed through a sharp-cutoff high-pass filter with a cutoff frequency of 160 Hz (corresponding to 40 Hz at recording speed). This procedure eliminated the noise below 40 Hz without affecting the signal information above 40 Hz. Figure 8 shows the frequency response of the filter used with all data except that from Series 900 shots.

2. The output of this filter was fed with suitable amplification into an analog-to-digital converter with a sampling rate of 15,754 Hz (3938.5 Hz at recording speed). This rate is considerably above the Nyquist rate, which thus allows for linear interpolation between sample points with negligible error. The digitized data samples were tested continuously against a preset threshold amplitude value, then were stored in a 64-word buffer in cyclic fashion. That is, when word 64 was stored, the sample following would be stored in word 1. This operation continued,
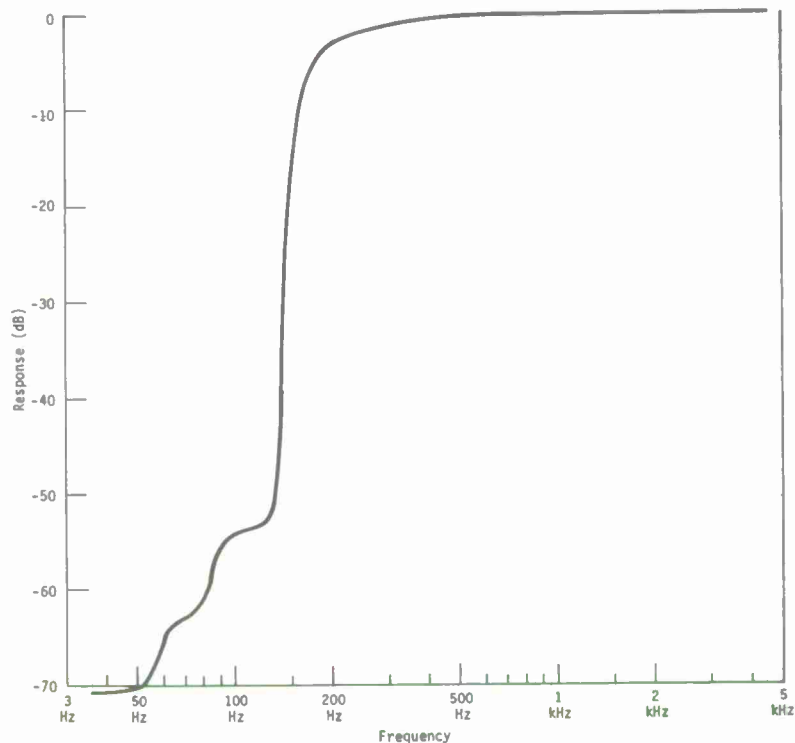
Fig. 8. Response of high-pass filter used in
data reduction. Because data records were
played back at four times the recording speed,
divide frequencies shown on the horizontal
scale by four to obtain filter effect at
recording speed.

always storing the most recently digitized 64 samples, until a value ex-
ceeding the threshold value was detected. This sample and all those fol-
lowing then were diverted into the 1024-word main storage array, begin-
ning at the 65th word. When the main array was filled, the 64 words
from the buffer were transferred into the main array in the correct se-
quence, thereby providing a short pretrigger sample of the signal. If
the computer operator was satisfied that the digitized signal was a valid
one, this 1024-word array was transferred to the magnetic tape bulk stor-
age (DECtape) of the computer in a format suitable for subsequent proc-
essing. The program then was reset to receive the next signal. All of
the shots received were translated into digital form in this manner. In
addition, for each series of shots, digital samples of noise only (taken
between shots) were recorded by artificially satisfying the threshold
logic at random points during each shot sequence. This noise analysis
was intended to give a measure of the available signal-to-noise ratio in
the data-reduction process.

3. Each shot was called back into core storage from the DECtape
and the pressure-time waveform was plotted on a cathode-ray tube (CRT)
graphic display to allow for positioning of time gates and to allow the
development of some insight into the physical processes of refelection.

11

Fig. 9. Pressure-time signatures and energy spectral densities of deep charges, Series 50, at Station A. For "incident" on the figure, read "direct."

Fig. 10. Pressure-time signatures and energy spectral densities of deep charges, Series 100, at Station B. For "incident" on the figure, read "direct.

Time gates were used to allow separation of the direct and reflected wave-
forms and to reduce the noise energy in the spectra. The left-hand sides
of Figs. 9-18 show the pressure-time signatures of all the shots recorded
and analyzed. The position of the time gates is shown on the signatures
with positions marked D indicating the gates for the direct signals and
positions marked R indicating the gates for the reflected signals.
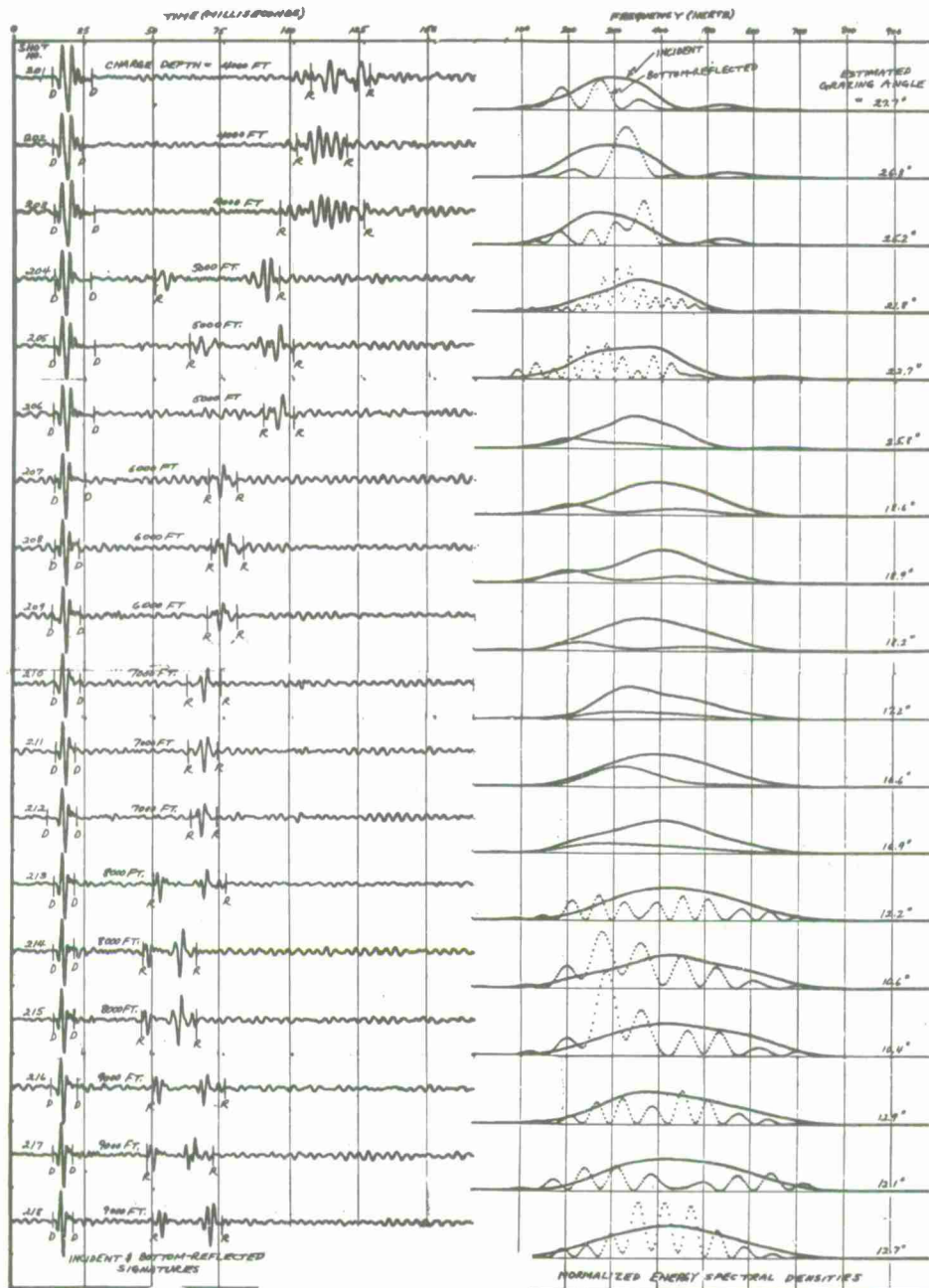
Fig. 11. Pressure-time signatures and energy spectral
densities of deep charges, Series 200, Station B. For
"incident" on the figure, read "direct."
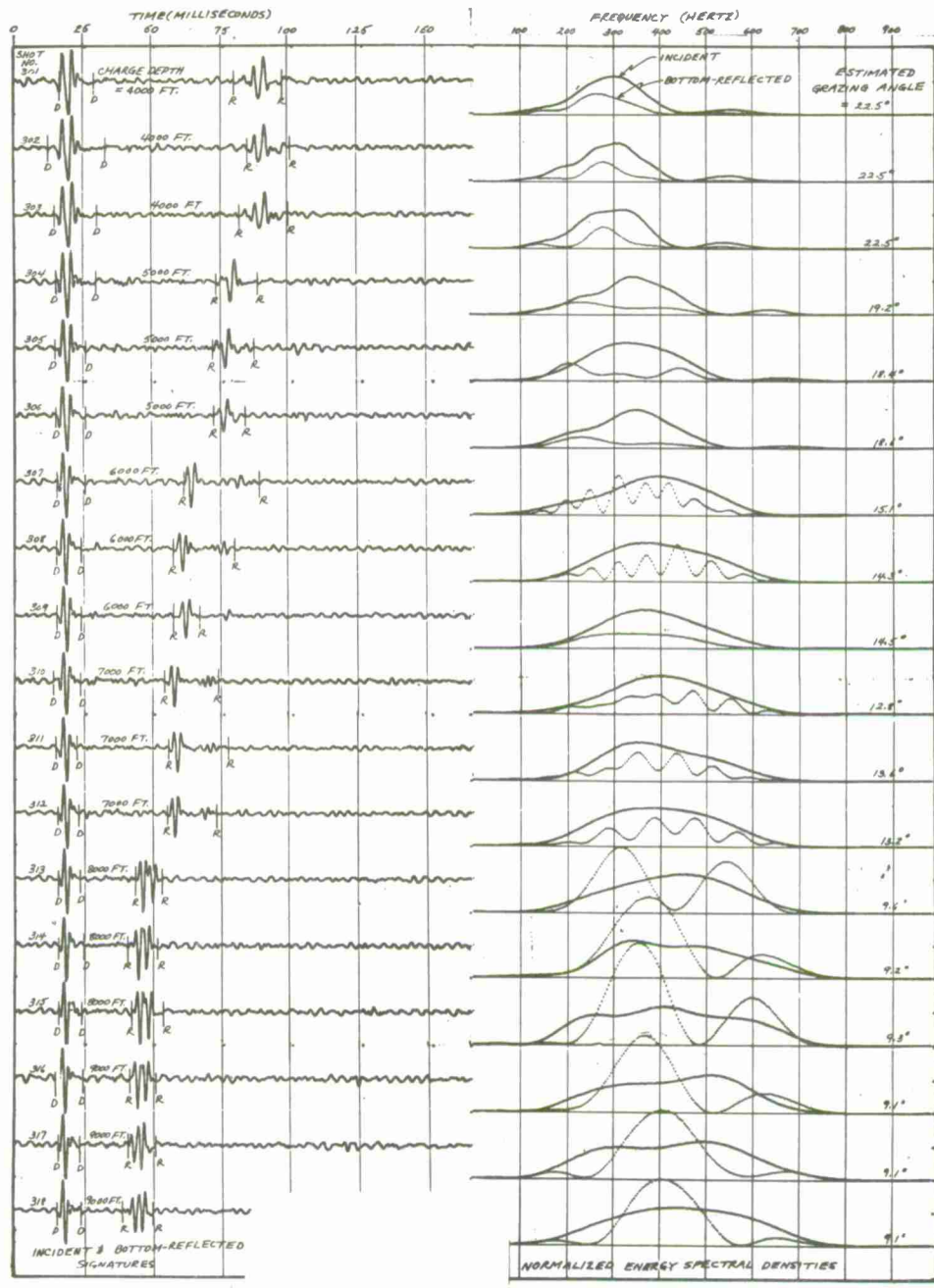
Fig. 12. Pressure-time signatures and energy spectral densities of deep charges, Series 300, Station B. For "incident" on the figure, read "direct."

Fig. 13. Pressure-time signatures and energy spectral densities of deep charges, Series 500, Station C. For "incident" on the figure, read "direct."
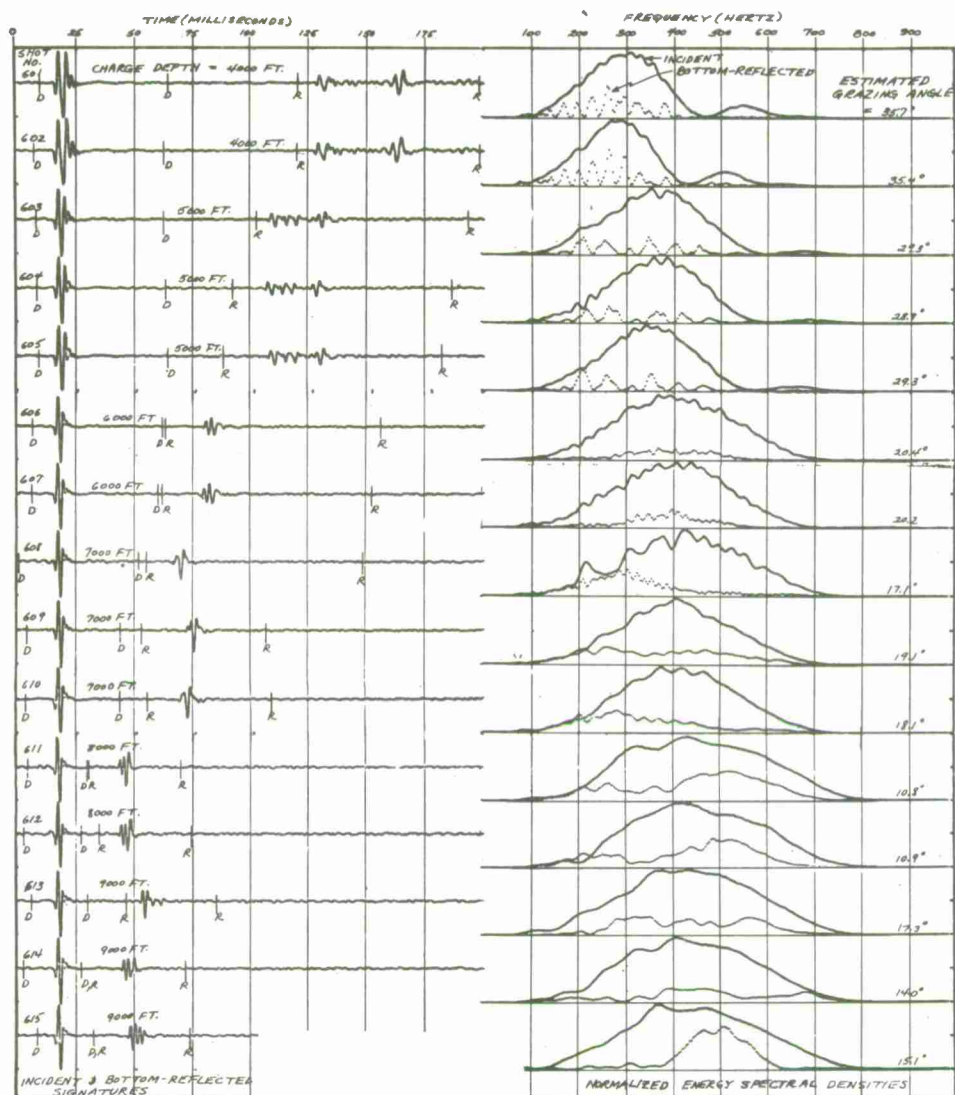
Fig. 14. Pressure-time signatures and energy spectral densities of deep charges, Series 600, Station C. For "incident" on the figure, read "direct."
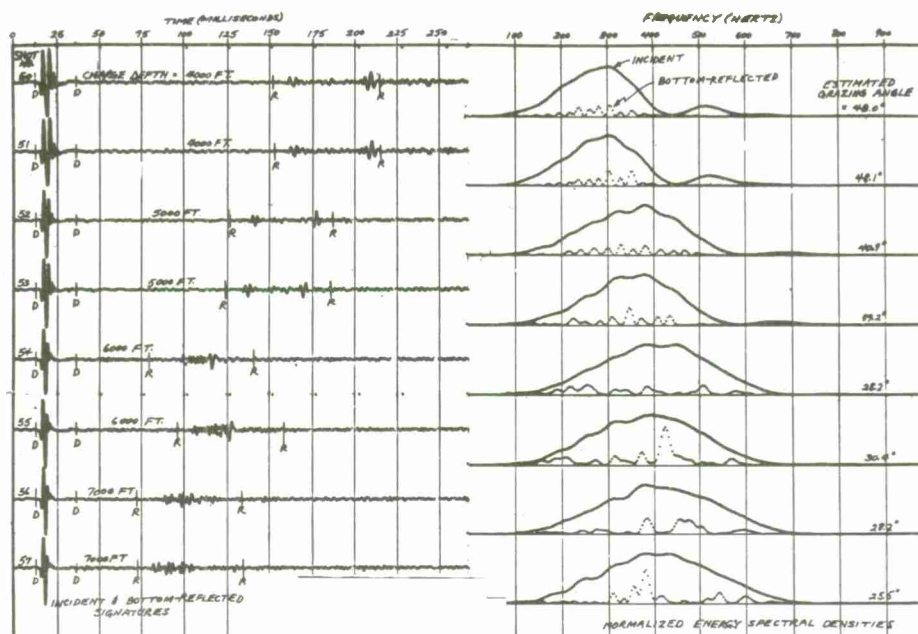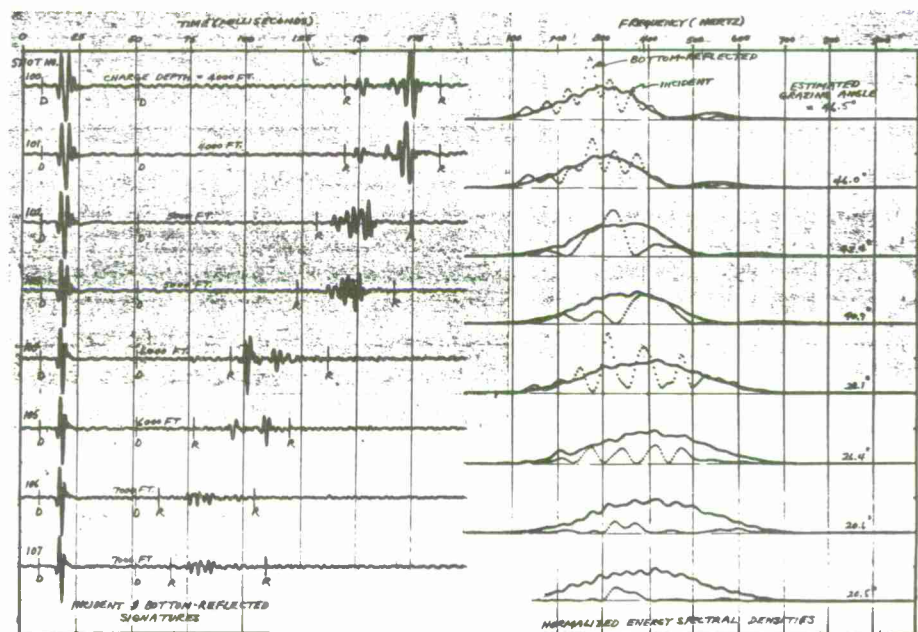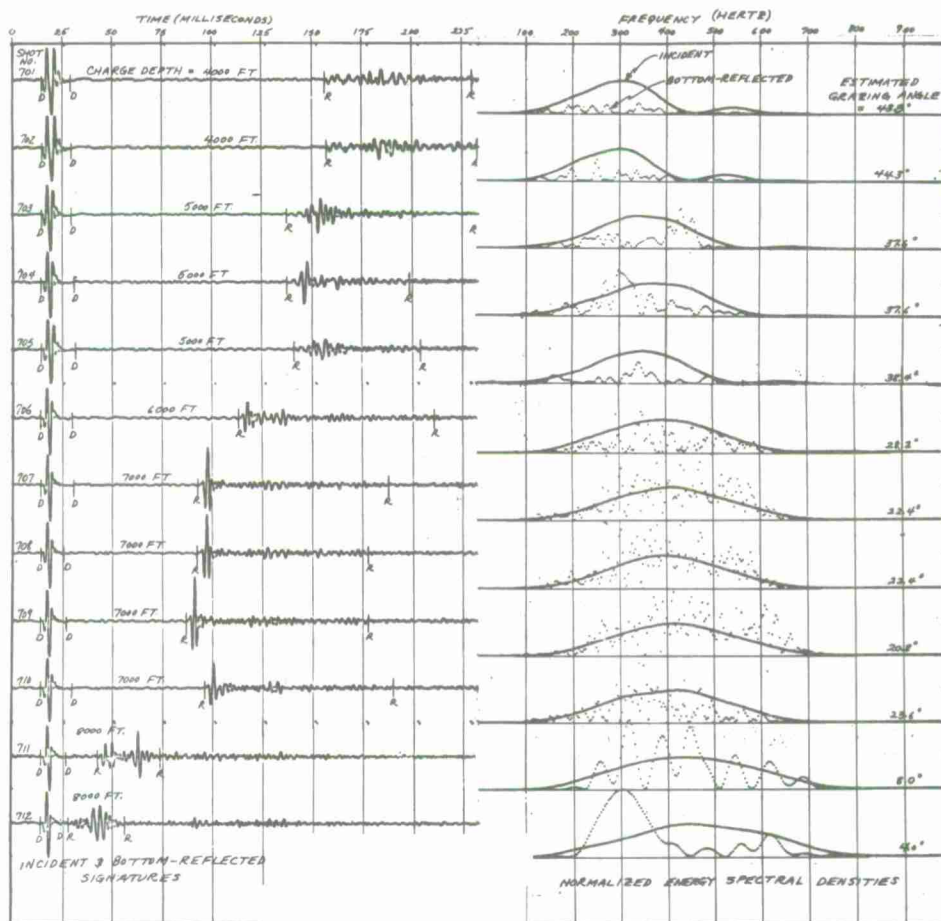
Fig. 15. Pressure-time signatures and energy spectral densities of deep charges, Series 700, Station D. For "incident" on the figure, read "direct."

17

Fig. 16. Pressure-time signatures and energy spectral densities of surface charges, Series 30, Station A. Shots 34-40, medium gain; shots 41-45, low gain. For "incident" on the figure, read "direct."

18

Fig. 17. Pressure-time signatures and energy spectral densities of surface charges, Series 350, Station B. Shots 355-362, low gain; shots 362-374, medium gain. For "incident" on the figure, read "direct."

19

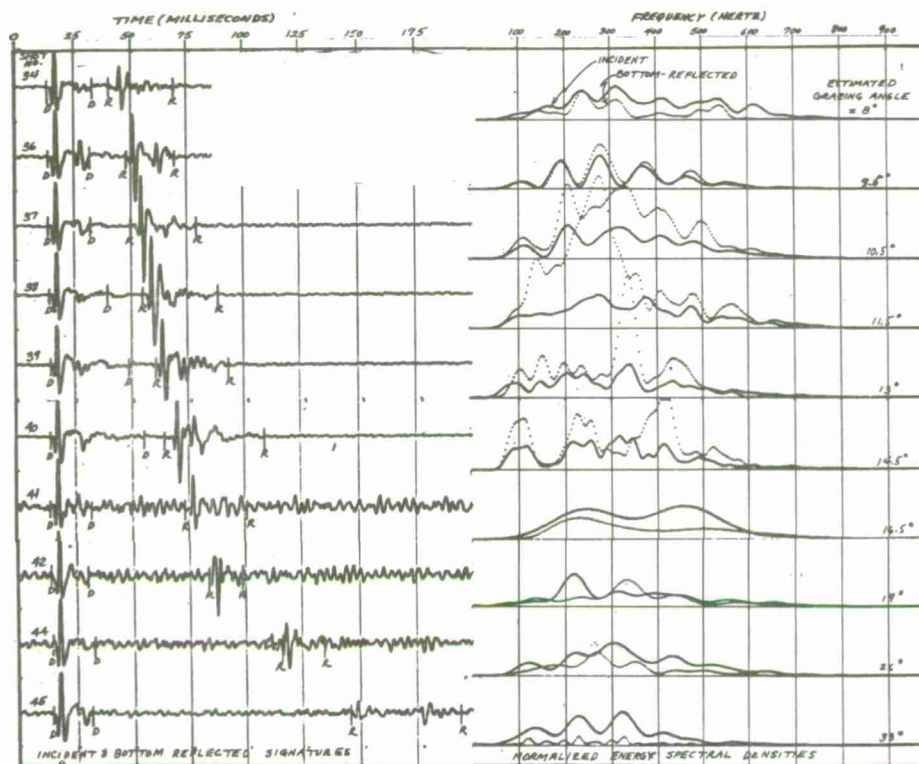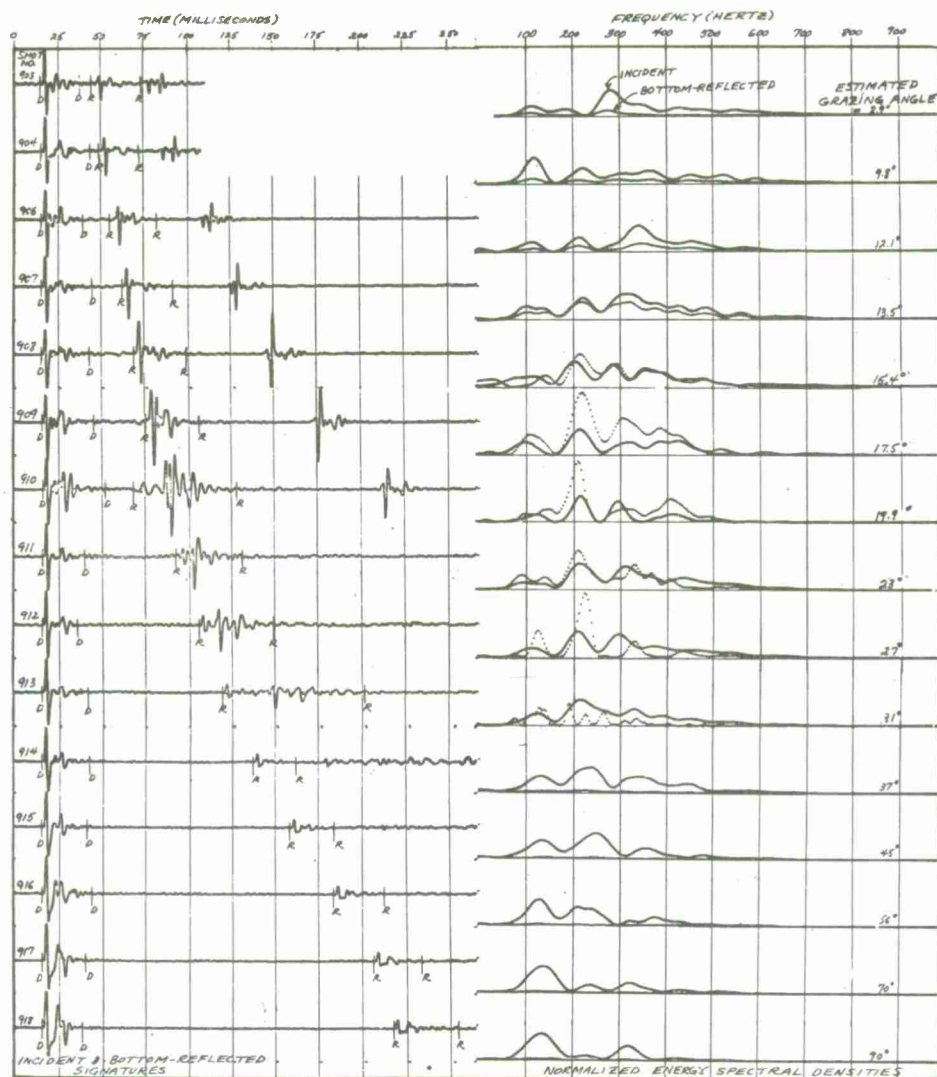Fig. 18. Pressure-time signatures and energy spectral densities of surface charges, Series 900, Station C. Shots 903-910, medium gain; shots 911-918, low gain. For "incident" on the figure, read "direct."

4. With the time gates as indicated, a fast Fourier transform (FFT) algorithm was used to generate separately the discrete Fourier transform (DFT) of the direct and the reflected signals. To do so, all values of the pressure outside of time gates were made equal to zero and the DFTs of the resulting waveforms were generated. Thus, two sets of DFT coefficients were generated for each shot, one for the direct signal waveform and one for the reflected waveform. These DFT coefficients are complex numbers representing the Fourier frequency coefficients of the gated waveforms. To obtain the energy spectral density (energy rather than power because the signals are transient), the sum of the squares of the real and imaginary components of each coefficient was obtained. These coefficients, which represent the energy at harmonics of the fundamental frequency (recording speed sampling frequency divided by 1024), are shown plotted on a linear scale on the right side of Figs. 9-18 for each of the corresponding appropriately gated time series on the left side of the figures. The solid curve is the energy spectral density of the direct signal; the dotted curve is the energy spectral density of the bottom-reflected signal. The two energy spectral densities (for each time series) are plotted on the same scale so that the square root of the ratio at a given frequency represents the amplitude of the reflection coefficient at that frequency.

5. An analysis of the effect that the constant sound speed gradient in the deep ocean has on the grazing angle of the bottom-reflected signal is given in Appendix A. This analysis is particularly pertinent to the deep-shot experiments because the experimental geometry is confined essentialy to that part of the ocean where the constant gradient exists. It is obvious that given the precise geometry associated with each shot, the sound speed at the bottom, and the speed gradient, the grazing angle and time difference of arrival of the direct and reflected signals can be calculated. Because the time difference of arrival also can be measured, the solution for the grazing angle is overspecified and mean-square methods could have been used to estimate the grazing angle; however, it was believed that a better estimate could be made by treating the parameter of least confidence as a variable and fixing all other parameters at their best estimates. It was felt that because of the unpredictable way in which the ocean currents would carry the deep charges as they sank, the horizontal range between the source and the receiver was the parameter of least confidence. Therefore, the estimated geometry of each shot (excluding the horizontal range), the estimated sound speed at the ocean bottom, and the estimated speed gradient were used in the equations developed in Appendix A to generate time difference of arrival of the direct and reflected signals as a function of grazing angle for each shot. The measured value of the time difference of arrival for a given shot then was used as an entry to the appropriate plot to determine the grazing angle for that shot. The estimated values of the grazing angle thus obtained are shown for each shot on Figs. 9-14. The estimated value for the grazing angle of the shots shown on Figs. 15-18 was

21

calculated by

$$\phi = \arcsin(t_d/2ch_r), \tag{7}$$

where t_d is the time difference of arrival of direct and reflected signals, c is the sound speed at the bottom, and h_r is the height of the receiving hydrophone from the bottom. This simplified means of estimating the grazing angle was used for all of the experiments involving surface shots because the experimental geometry was not confined to that part of the ocean where a constant sound speed gradient could be assumed. The estimate was used for the Series 700 deep shots because lack of knowledge of the relative position of the receiving ship with respect to the anchor at the time of the experiment introduced considerable uncertainty as to the bottom slope as well as the horizontal separation.

Summary of Data

All data acquired and reduced are shown in Figs. 9-18, with the left side of the figures showing the pressure-time history of the direct and reflected signals and gating points used for data reduction. The direct signal gates are marked with a D and the reflected signal gates are marked with an R. The right-hand side of the figures show the energy spectral densities as calculated from the FFT. The solid curves are the energy spectral densities of the direct signals; dotted lines are the energy spectral densities of the reflected signals. All of the data are shown for two reasons: (1) so that individual readers may interpret both the raw data and the processed data for themselves, and (2) to assist in the critique of the experiments that will be discussed in a subsequent section.

A summary of the data from the deep-shot experiments will be presented first, with a summary of the surface-shot experiments following. Figure 9 shows the pressure-time signature and the associated energy spectral densities of the direct and the bottom-reflected signals for the Series 50 shots. The bathymetry and relative geometry of this sequence are shown in Fig. 5. Although there were only 8 shots in this particular sequence, two things are apparent from the data. First, the localized bottom loss was considerably higher (for all grazing angles) at Station A than that at any other station. Second, there are undoubtedly subbottom reflections that interact with the water-sediment reflections to give large variations of the reflection coefficient with frequency. Some of these variations (the energy spectral density of the reflected signals in shot 52, for example) are sinusoidal-like variations that are characteristic of coherent signals separated in time. There are others, such as shot 55, that show an apparent resonance effect in the bottom-reflected energy.

Figures 10-12 show the pressure-time signature and the associated energy spectral densities of the deep-shot data collected at Station B. The bathymetry and relative geometry of the various shot sequences are shown in Fig. 6. Figure 10 shows the data from a sequence of deep shots dropped from the ship where the shot separation from the receiving hydrophone was less than desired because of the short anchor scope. These data show that virtually all of the energy that was incident on the bottom at grazing angles greater than about 28 deg was reflected from the water-sediment and subbottom structure. As the grazing angle became less than 28 deg (with the deeper shots), losses in the bottom apparently became much greater. For the shallowest shots (shots 100 and 101), it appears that most of the energy was reflected from the subbottom structure rather than from the water-sediment interface. Coherence between these subbottom reflections and the direct signal was high. One shot (shot 104) did show a strong reflection from the water-sediment interface. Again, interaction between the water-sediment reflection and the subbottom reflections was pronounced in the energy spectral densities of the bottom-reflected signals. Losses at grazing angles of approximately 20.5 deg appeared much greater than for the steeper grazing angles. Also, a resonance effect between 300 and 400 Hz can be noted in the energy spectral densities of the reflected signals at this grazing angle.

As stated earlier, additional deep-shot data were collected at this station by using a motorized raft dispatched from the ship to drop the charges. Figures 11 and 12 show the pressure-time signatures and energy spectral densities of the shot sequences from the raft. One of the differences between these two shot sequences and those of Figs. 9 and 10 is the poorer signal-to-noise ratio, which makes the data much less reliable. This poorer signal-to-noise ratio is due to the greater separations between the shot and the receiving hydrophone. Shots 201-203 of Fig. 11 show reflections from a complex bottom structure with correspondingly large variations in the energy spectral densities of the bottom reflections. Shots 204 and 205 show apparent precursors to the reflection from the water-sediment interface. For shot 204, this precursor is coincident in time with the direct arrival at a bottomed hydrophone that was being monitored. It is possible that it could be due to crosstalk between the two monitoring channels. This explanation does not apply to the precursor that appears on shot 205; however it could be due to a random spike in the background noise. For shots 206-212 corresponding to grazing angles of 16.6-25.8 deg, there is apparently only a reflection from the water-sediment interface. At smaller grazing angles (shots 213-218), the subbottom reflection again appears in the pressure-time signature. This rather peculiar pattern of a subbottom reflection being absent for grazing angles between approximately 16.5 deg and 25 deg but present for grazing angles greater than 25 deg and less than 16.5 deg might be explained by the existence of an "angle of intromission" for the sediment-subbottom interface corresponding to this range of grazing angles for the water-sediment interface. Figure 12 shows results similar to those of Fig. 11. It should be noted (from Fig. 6) that the Series 200 and 300 shot sequences involve only slightly different portions of the bottom. A significantly different part of the bottom is involved for the Series 100 shots.

At Station C, a 15-dB attenuator in the low-gain preamplifier was removed, resulting in generally improved data for the deep-shot experiments. Also, at Station C, anchor scope was large enough to permit all deep shots to be dropped from the ship. Figures 13 and 14 show the pressure-time signatures and the energy spectral densities for the deep-shot experiments at Station C. Figure 7 shows the area bathymetry and the relative geometries associated with the two shot sequences. On both Figs. 13 and 14, reflections from the subbottom disappear at angles below approximately 20 deg, apparently because of an angle-of-intromission effect at the sediment-subbottom interface rather than a critical angle effect at the water-sediment interface. At the lowest grazing angles on Fig. 14 there is what appears to be both water-sediment interface reflections and sediment-subbottom interface reflections. Shots 512 and 514 of Fig. 13 are worth noting. Shot 512 shows an energy spectral density curve for the reflected signal that is almost identical in shape to the energy spectral density curve of the direct signal, but with the reflected energy greater than the direct signal. This result could be caused by the focusing effect of curvature in the water-sediment boundary. The energy spectral density curve of the reflected signal of shot 514 is almost an exact overlay of the energy spectral density curve for the direct signal. Also, shots 503 and 504 from Fig. 13 are remarkably similar. Again, in both figures, there are regular interference-type patterns in the energy spectral densities of the reflected signals when both sediment and subbottom reflections occurred.

Figure 15 shows the pressure-time signatures and the energy spectral densities for the deep-shot experiments at Station D. The bottom slope at Station D was approximately 10 deg; however, no bathymetry is shown because the ship's position relative to the anchor was not logged. The bottom reflection at this station was somewhat different from that for other stations in that reverberation effects were quite high, probably because of scattering within the sediment layer. Shots 707-709 are particularly interesting in this sequence because of the large coherent reflection from the water-sediment interface followed by reverberation from within the sediment layer. Note the scatter in the energy spectral density curves that is a result of including the reverberation in the gates for the reflected signal.

One quality that should be pointed out for all of the deep-shot data is that although repeatability of reflected signals is observed when geometries are sufficiently close, small changes in the geometry can produce strikingly different results. It should be noted also that direct signals (for similar depths) are repeatable to a remarkable extent. Also note, in all cases, the upward shift of the maximum for the energy spectral density of the direct signal with increased depth.

The surface-shot experiments were planned to produce a higher level of energy in the source at the lower frequency. It was felt that both the size of the bubble and the bubble frequency would not allow the desired energy at lower frequencies, particularly for the very deep shots.

Consequently, it was planned to use charges detonated just below the surface so that the bubble would vent on the first bubble expansion as described under "General Description of Experiments." This procedure should provide for a larger bubble and consequently more low-frequency energy. Venting of the bubble on the first expansion would avoid bubble oscillations that would extend the time duration of the source and thus complicate the temporal separation of the direct and reflected arrivals. Figures 16-18 show the pressure-time signatures and the energy spectral densities of three sets of surface shot experiments conducted at Stations A, B, and C. Bathymetry and shot geometries for these stations are shown in Figs. 5-7. Data Stations A and B (Figs. 16 and 17) were poor because of the variation in signal levels and the 34.3-dB difference in gain between the low- and medium-gain channels. Control of the signal levels on the magnetic tape recorder thus was almost impossible; when the medium-gain channel was overloaded, the signal-to-noise ratio on the low-gain channel was still very small. This situation was corrected before anchoring at Station C by removing a 15-dB attenuator pad from the low-gain channel; consequently, data at Station C (Fig. 18) were much better. Also, data from Figs. 16 and 17 were played through the filter of Fig. 8; data from Fig. 18 were not.

The signal-to-noise ratio of shots 41-45 (low-gain channel) of Fig. 16 is so poor that only a qualitative assessment of the results can be made. There does appear to be generally more energy reflected than for the deep-shot experiments at the same station. Shots 37-40 (medium-gain channel) are obviously overloaded (probably in the recorder rather than the telemetry); however, it is felt that the overloading was not due to exceeding the maximum frequency deviation of the voltage-controlled oscillator (VCO), but rather to frequencies being generated outside the FM subcarrier band. This type of overloading is unusual and probably occurs on the direct signal rather than the reflected signal. Shot 36 also probably is slightly overloaded, but it does appear to represent a Rayleigh-type reflection, with the energy spectral densities of the direct and reflected signals being virtual overlays. The grazing angle associated with shot 34 is such that total reflection of the direct signal might be expected. It is suggested that the divergence effect (see Appendix A) may be the cause of the reduced level of the reflected signal.

Figure 17 shows the pressure-time signatures and the energy spectral densities of the shallow-shot data collected at Station B. Again the data collected on the low-gain channel (shots 355-361) have inadequate signal-to-noise ratios to be of practical use. Shots 362-373 show what appears to be classic Rayleigh reflection. There may be some slight overloading effect in some of these shots and there also may be slight focusing or defocusing effects produced by bottom curvature. There also may be a divergence effect in shot 373. In general, however, the energy spectral densities of the reflected and direct signals show remarkable agreement. Shots 371-374 show a secondary reflection possibly from a second portion of the bottom that provides a specular reflection path to the receiving hydrophone. This secondary reflection was included in the gated reflected signals for shots 372 and 373, which is the reason for the

25

scatter in the energy spectral density curves for the reflected signals in these two shots. Shot 374 apparently has a grazing angle so small that the direct and primary reflection signal can not be separated in time.

Figure 18 shows the pressure-time signatures and the energy spectral densities of the shallow-shot data collected at Station C. These data were recorded with the 15-dB attenuator pad removed from the low-gain channel. Data recorded on this channel show a much improved signal-to-noise ratio. Also, these data were *not* played back through the filter of Fig. 8. Although the pressure-time signatures of Fig. 18 are very clean, there are some problems in interpreting the results. The two reflections associated with shots 903-910 are thought to have come from two separate portions of the bottom, each of which provided a specular reflecting surface to the hydrophone receiver. However, note shot 908, where the first reflection is almost identical to the direct signal. The second reflection is almost identical to the direct signal except with a 180-deg phase reversal. This fact implies that the first reflection is occurring at a grazing angle near the critical angle (because of the near-unity reflection coefficient) and with almost complete phase coincidence. The second reflection then must occur for a very small grazing angle to account for the 180-deg phase reversal. For a small grazing angle to exist with the time separation as observed between the direct and second reflected signal, the separation between the receiving hydrophone and the plane of the second reflection surface must be very large (about 15000 ft). From examining the bathymetry of Fig. 7, it does appear posssible for the peak to the right of the track of the ship dropping charges to provide such a reflecting surface. In any case, shot 908 represents an unusual type of bottom-reflection signature. For shots 903-908, both the primary and secondary reflections show a decrease in reflection coefficient with decreasing grazing angle. This decrease could be due to divergence effects as discussed in Appendix A, even though the calculations seem to indicate that divergence effects should not be so pronounced. Data for the direct arrival from shots 909 and 910 appear to be overloaded by frequencies generated outside the recorder (or telemetry) FM subcarrier band; however, there is an interesting precursor associated with the first reflected arrival of shot 910. It is believed that the precursor is due to a surface wave propagating along the bottom at a speed higher than that in the water (Stoneley wave). For the higher grazing angles (shots 912-918), there is the obvious transmission of energy into the bottom and subsequent reflections from either back-scattering in the sediment or from subbottom structure.

It is apparent from the incident energy spectral densities calculated for all of the surface-shot experiments that relatively larger amounts of low-frequency acoustic energy in the source were obtained with the surface charges than with the deep charges. Considerable fluctuation appears in the energy distribution as a function of frequency for the shallow shots and there was also a distinct directional effect. For example, note the pressure-time waveform of shot 918 (Fig. 18) for a shot almost directly over the receiving hydrophone and the waveform of shot 903 which

was 7-8 nautical miles away. There is little reason to expect repeat-ability of results insofar as energy spectral distribution is concerned, however, because of probable random variations associated with the for-mation of the plume and its effects produced by the random "water sur-face state" at detonation. The directional properties of the surface source probably are due to the nonsymmetrical properites of the water cavity that exists when the bubble vents. In other words, while the low-frequency energy is enhanced over that for a deep charge, the uncertain-ties that are introduced because of directivity and the random nature of the water surface make the surface source very difficult to characterize. One other general point in regard to the surface shot experiments is the increased problem of obtaining good recordings of the data with the con-stant changing of signal levels as the range to the shot is changed. Also, it is quite apparent that in the shallow-shot experiments different portions of the bottom were involved for each grazing angle observed.

Critique of Experiments

One of the primary purposes of this report is to provide some docu-mentation of the problems associated with this type of experiment and the most common mistakes that can be made. This statement is not meant to imply that the work done was not considered successful, but rather that much may be learned from the exposed inadequacies of the experiments as conducted. Most of the deficiencies of the data-acquisition system arose from design compromises necessitated by using the same system in other planned experiments; however, the purpose of this section is not to justify but to criticize.

The most important deficiency of the bottom reflectivity experiments was lack of high-fidelity recordings of all data with good signal-to-noise ratios. The reasons for this lack are:

1. Inadequate over-all dynamic range for the data-acquisition system.

2. Failure to make full use of the dynamic range that was available by appropriately adjusting the recording level topside.

3. Failure to control the frequency of the data collected so that distortion in the FM telemetry and/or the FM recording would not be pro-duced by frequencies generated outside the subcarrier bands of the telem-etry and recording system.

The dynamic range of the magnetic tape recorder used was 35-40 dB. An attempt was made to extend this dynamic range by providing three staggered-gain channels to be recorded on three separate channels of the tape recorder. (Three other channels were used to record signals from a bottomed hydrophone, the results of which are not included in this re-port.) At the first two stations (A and B) there was a nominal 35-dB gain separation between the low-gain channel and the medium-gain channel and a nominal 20-dB gain difference between the medium-gain channel and the high-gain channel. Almost all of the useful data were on either the

low-gain channel or the medium-gain channel. (Actually, the high-gain channel was planned principally for ambient noise experiments which were a part of the over-all exercise.) With the 35-dB gain difference between the medium and low-gain channels, much of the data were overloaded on the medium-gain channel and recorded with a poor signal-to-noise ratio on the low-gain channel. The gain difference between the medium and low-gain channels was reduced from 35 dB to a nominal 20 dB by removing a 15-dB attenuator pad from the low-gain channel before collecting data at Stations C and D. Even with the 20-dB gain difference, some difficulties still existed in obtaining as wide a dynamic range as was desired.

One factor not adequately considered in the experimental design was the transient nature of the signal; that is, a relatively high amplitude in the initial portion of the signal with subsequent decay of the amplitude in later portions of the signal. This condition was present in both reflected and direct signals, but was more pronounced in the direct signals. Also, the amplitude of the reflected signals was down by as much as 20 dB in many cases from the amplitude of the direct signals. Thus, even with full utilization of the dynamic range of the tape recorders, the 35-40 dB available was only marginally adequate. One possible way to circumvent this problem would have been to digitize the high-level portions of the signal from the low-gain channel and the lower level portions from the medium and/or high-gain channels and multiplex the results, using appropriate weighting factors. This procedure was attempted with some of the data, but it was not successful because the phase responses of the various gain channels were not adequately matched. Because the dynamic range of the analog tape recorder was the limiting factor, immediate analog-to-digital conversion of data received topside and the use of digital recording would have been more appropriate. Such equipment was available on the ship, but it was not used because no digital playback facilities were available and thus appropriate interaction could not be maintained with the experiments. The changing levels of the signals to be recorded, particularly the data from the surface-shot experiments, made this interaction absolutely essential.

Certain procedures available topside could have been utilized more fully to control the dynamic range problem. Because the overload level of the telemetry channels was 10 dB above the overload level of the recorder, more topside use of attenuator pads could have been made to control the recording levels. Also, the dynamic range of the telemetry channels was much greater than that of the recorder. Additional amplification at topside (if amplifiers had been available) could have been used to control the recording levels. In retrospect, what would have been desirable is a topside amplitude control panel consisting of both attenuator pads and amplifiers.

In any type of FM system, there are two principal elements by which distortion of the signal may be introduced. One of these is possible nonlinearity of the voltage-controlled oscillator (VCO) and the other is the generation of frequencies outside the subcarrier band of the FM system. Excessive input signal amplitudes, regardless of frequency, may produce distortion in one or both elements. Distortion due to excessive

28

signal amplitudes generally is easy to recognize and is the more common type of distortion. On the other hand, frequencies that are too high may easily generate frequencies outside the subcarrier band, even though their amplitudes are small enough to insure linear operation of the VCO. If the amplitude and phase response of the subcarrier filter were perfectly symmetrical about the center frequency, the type of distortion that would result would be equivalent to that of a low-pass filter. Because this type of symmetry generally is not achievable with the bandpass subcarrier filter (particularly in the attenuation band), the type of distortion that results is unpredictable and quite frequently difficult to recognize. An example of this type of distortion is seen in the direct signal of shot 910, Fig. 18. In this particular signal, the effect appears to be a compression of the signal amplitude without noticeable distortion of the signal waveform. One of the serious inadequacies of the data acquisition and recording system for the bottom reflectivity experiments was failure to provide adequate filtering to prevent this type of distortion. The demodulators in the telemetry channel were followed by 300-Hz low-pass filters; however, these filters had only a 6-dB/octave cutoff rate. The sharp rise time associated with the signals (especially the direct signal) shows that the filtering was not adequate for the recording system. A sharp-cutoff low-pass filter should have been placed immediately after the suspended hydrophone preamplifier.

The preceding paragraphs have dealt with the shortcomings of the data-acquisition and recording system. There were also other deficiencies in the experimental design that, for the most part, were unavoidable; nevertheless, they should be pointed out. Control over the geometry was inadequate in the experiments. For the deep shots, discrepancy between the actual and the designed detonation depths probably was as large as 200-300 ft, so that no really precise knowledge of the detonation depths existed. Also the charges undoubtedly were carried by ocean currents to considerable horizontal distances from their drop points. In addition to a lack of precise information on the relative geoemetry associated with the charge detonation positions, high-resolution bathymetry necessary to make accurate estimates of the grazing angles involved was lacking. For the shallow-shot experiments, both the inadequate bathymetric information and the lack of information for appropriate ray tracing also led to only rough estimates of the grazing angle. The extreme bottom roughness at the data-collection sites further complicated the problem. A more desirable experimental design should include methods for a more direct measure of the grazing angle.

Proposed New Experiments

The success of the bottom reflectivity experiments described in this report, particularly for some of the adverse conditions under which the experiments were conducted, seem to warrant the proposal of new experiments to correct the deficiencies discussed in the previous section. A detailed design would depend upon the manpower and money available for

the experiment and thus would be premature at this time; therefore, it is the purpose here just to provide some basic guidelines to such an experimental design.

The principal guidelines for the design of new bottom-reflectivity experiments are:

1. Select a site where the bottom is relatively flat and where as much general information as possible is available about the area. Conduct a highly detailed bathymetric survey of the area in advance.

2. Record data from at least two hydrophones suspended off the bottom and vertically separated. The vertical separation should be sufficient to allow determination of the vertical angle of arrival for the direct and the reflected signals on the basis of the time difference of signal arrivals at the two hydrophones.

3. Exercise extreme care to insure the highest quality data recordings with the highest possible signal-to-noise ratios. A dynamic range of 60-80 dB is highly desired. If a ship-anchored system is used, as in these experiments, consider digital telemetry and/or digital recording. Give some consideration also to a small recoverable self-contained data-acquisition and -recording package that would operate at depth. This would present problems in the control of the experiment, but would maximize the amount of data that could be collected as a function of ships' time available.

Consider also, in any new experiments, the estimation of bottom sediment parameters such as density, sound speed, and attenuation from the acoustic measurements made. Methods for achieving this are discussed briefly in Appendix B.

Conclusions and Recommendations

The experiments were a "qualified" success. Although quantitative results were not obtained to the extent desired, qualitative results were obtained on the complexity of bottom effects. A tentative conclusion is that the development of deterministic models of localized bottom effects will be impossible, particularly where bottom topography is rugged. Prediction of statistical trends may be practical.

Conclusions on the experimental procedures were that they offer considerable potential, particularly in regard to data-reduction techniques.

It is recommended that the experiments be repeated in an area where more control can be exercised over the experimental geometry after data-acquisition deficiencies associated with the experiment have been corrected.

Acknowledgments

References

[1] A. Berman and A. N. Guthrie, "On the Medium from the Point of View of Underwater Acoustics," J. Acoust. Soc. Am. 51, 994-1009 (1972).

[2] A. O. Williams, Jr., "Propagation," J. Acoust. Soc. Am. 51, 1041-1048 (1972).

[3] E. L. Hamilton, "Sound Attenuation in Marine Sediments," Naval Undersea Center Report TP 281, Mar 1972.

[4] I. Tolstoy and C. S. Clay, *Ocean Acoustics* (McGraw-Hill Book Co., New York, 1966).

[5] O. F. Hastrup, "Digital Analysis of Acoustic Reflectivity in the Tyrrhenian Abyssal Plain." J. Acoust. Soc. Am. 47, 181-190 (1970).

Appendix A
THE EFFECTS OF REFRACTION ON
BOTTOM-REFLECTION GRAZING ANGLE AND DIVERGENCE
IN THE VERY DEEP OCEAN

Introduction

In the very deep ocean (depths greater than 1500 m), variations of
salinity and temperature as a function of depth are very small so that
sound speed as a function of depth is almost exclusively a function of
pressure alone. Because sound speed variations are linearly related to
pressure and pressure is linearly related to depth, a constant sound
speed gradient exists. The most generally accepted value for the sound
speed gradient in the deep ocean is 0.017 s^{-1} (or meters/second per
meter).

It is a well known fact that a given ray path in a constant sound
speed gradient field follows the arc of a circle whose radius is given
by

$$r = c/(g \cos \beta), \qquad\qquad (A1)$$

where c is the sound speed at any given point on the ray path, β is the
elevation (or declination) angle of the ray path from the horizontal at
the same point, and g is the sound speed gradient. It is necessary to
develop some other relationships involving refraction in a constant
gradient field before actually looking at the specific effects on bottom-
reflection grazing angles and divergence. From Fig. A1, the radius of
the ray path is given by

$$r = c_1/[g \cos(\theta - \Delta)], \qquad\qquad (A2)$$

where c_1 is the sound speed at point 1, θ is the angle of elevation to
point 2 from the horizontal, Δ is the angle the refracted ray makes with
the straight line between points 1 and 2, and g is the sound speed
gradient. Also, from Fig. A1,

$$r = S/(2 \sin \Delta), \qquad\qquad (A3)$$
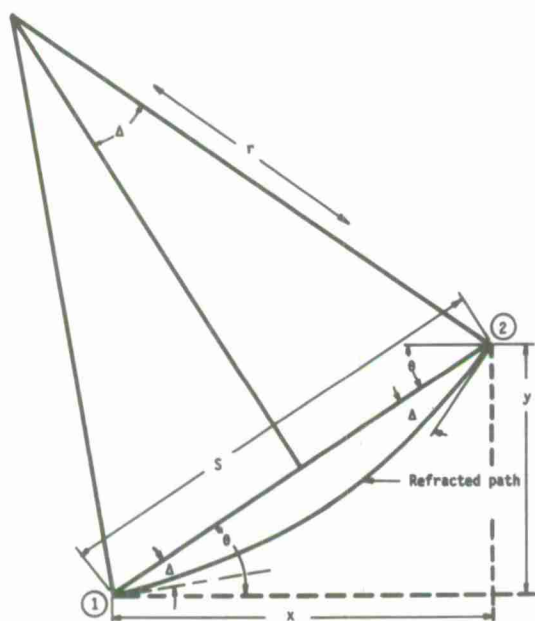
Fig. Al. Refraction of bottom-
reflected signal by constant
sound speed gradient.

where S is the slant range between points 1 and 2. Combining Eqs.
(A2) and (A3) produces

$$S/(2 \sin \Delta) = c_1/[g \cos(\theta - \Delta)],$$

and solving this for cot Δ yields

$$\cot \Delta = [2c_1/(Sg \cos \theta)] - \tan \theta$$

or

$$\cot \Delta = 2c_1/gx - y/x = (2c_1 - gy)/gx = 2c_m/gx, \qquad (A4)$$

where $c_m = c_1 - g(y/2)$ is the sound speed at the midpoint of a line
between points 1 and 2. Equation (A4) can be rewritten as

$$\tan \Delta = gx/2c_m,$$

or

$$\Delta = \arctan (gx/2c_m). \qquad (A5)$$

*Equation (A5) states that the deviation angle of the refracted signal
from the straight-line geometry is defined by the horizontal separation
between two points, the sound speed at a point midway between the two
points, and the speed gradient.*

The travel time between points 1 and 2 can be calculated by consider-
ing an incremental element dL along the arc of the ray path. Associated
with this incremental arc is an incremental angle dβ. Therefore, dL = rdβ.
The travel time along the incremental arc is given by

$$dt = rd\beta/c, \tag{A6}$$

where c is the actual sound speed at that point on the arc. From Eq. (A1), c is given by

$$c = rg \cos \beta. \tag{A7}$$

Substituting this expression in Eq. (A6) yields

$$dt = rd\beta/(rg \cos \beta) = d\beta/(g \cos \beta). \tag{A8}$$

From Fig. A1 and Eq. (A8), the travel time between points 1 and 2 is given by

$$t = (1/g) \int_{\theta-\Delta}^{\theta+\Delta} d\beta/\cos \beta = (1/g) \ln\left[\tan(\tfrac{1}{4}\pi + \tfrac{1}{2}\beta)\right] \Bigg|_{\theta-\Delta}^{\theta+\Delta}$$

$$= \frac{1}{g} \ln\left(\frac{\tan(\tfrac{1}{4}\pi + \tfrac{1}{2}\theta + \tfrac{1}{2}\Delta)}{\tan(\tfrac{1}{4}\pi + \tfrac{1}{2}\theta - \tfrac{1}{2}\Delta)}\right). \tag{A9}$$

which reduces to

$$t = \frac{1}{g} \ln\left(\frac{\cos \theta + \sin \Delta}{\cos \theta - \sin \Delta}\right). \tag{A10}$$

The travel time obviously is independent of direction of travel along the arc.

Effects of Refraction on Bottom-Reflection Grazing Angle

Figure A2 is a geometric representation of the specific problem of concern. The desired parameters are defined as follows:

h_r height of receiver above bottom

d_r depth of water at receiver

h_s height of source above bottom reflection point

d_b depth of bottom reflection point

d_s depth of source below ocean surface

x horizontal separation of source and receiver

x_r horizontal separation between receiver and point of reflection from bottom

x_s horizontal separation between source and point of reflection from bottom

θ angle of declination or elevation (from horizontal) between source and receiver

34
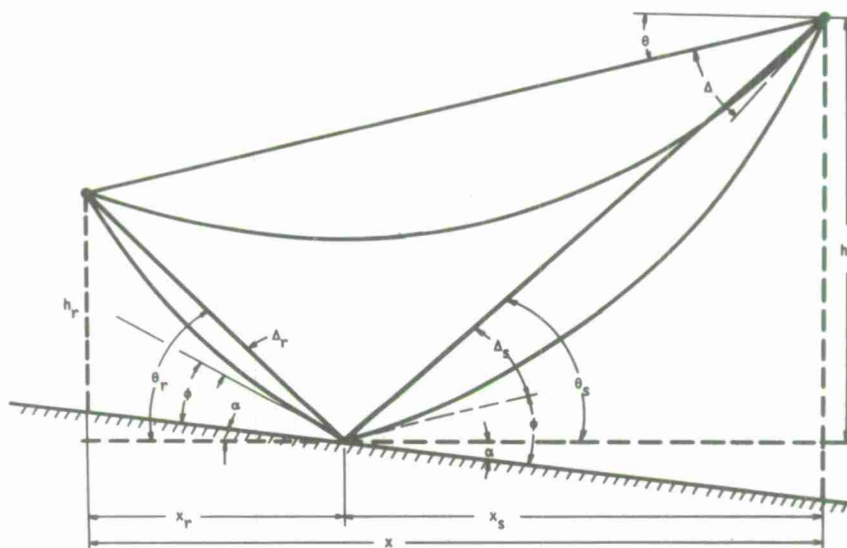
Fig. A2. Effect of refraction on bottom-reflection
grazing angle.

θ_r angle of declination (from horizontal) between receiver
and point of reflection from bottom

θ_s angle of declination (from horizontal) between source
and point of reflection from bottom

Δ angle of perturbation from straight-line geometry pro-
duced by refraction of direct path

Δ_r angle of perturbation from straight-line geometry pro-
duced by refraction of the path from the bottom reflec-
tion point to the receiver

Δ_s angle of perturbation from straight-line geometry pro-
duced by refraction of the path from the source to the
bottom reflection point

g sound speed gradient (constant in problem)

c_b sound speed at ocean bottom directly below receiver

c_r sound speed at bottom reflection point

α angle of slope of bottom (positive for down slope from
receiver)

ϕ grazing angle

t_d time difference of arrival for direct and reflected paths

The calculation procedure is to set h_r, d_r, c_b, g, α, and d_s as
problem constants. For a desired value of ϕ, required values of x_r and

35

Fig. A3. Expanded version of ray path from source to bottom.

Δ_r may be computed by a iterative process that provides very rapid convergence. From these values, θ_r, $(\phi - \alpha)$, and c_r can be computed. The terms $(\phi - \alpha)$, c_r, and g define the arc of a circle (and its center) on which the source must lie. For a given h_s, the required values of x_s and x then can be calculated. With this information, θ, θ_s, θ_r, Δ, Δ_s, and Δ_r can be evaluated, and the time difference of arrival between the direct and the bottom-reflected signals can be computed.

The detailed procedure is:

Given: h_r, c_b, g, and α; select a desired value of grazing angle ϕ. With $\Delta_r = 0$, compute

$$x_r = h_r / [\tan(\alpha + \phi + \Delta_r) - \tan \alpha]. \tag{A12}$$

Compute a new Δ_r from

$$\Delta_r = \arctan[gx_r / (2c_b - gh_r + gx_r \tan \alpha)]. \tag{A13}$$

With this value of Δ_r, compute a new value for x_r from Eq. (A12). With the new value of x_r, compute a new value of Δ_r from Eq. (A13). Repeat this process until the difference between the new value of Δ_r and the previously computed value is negligible.

Compute

$$\theta_r = \alpha + \theta + \Delta_r. \tag{A14}$$

Because the angle of incidence is equal to the angle of reflection, the elevation angle of the source ray (from the horizontal; see Fig. A3) is given by $(\phi - \alpha)$. The radius of curvature of the path from the source to the bottom is given by Eq. (A1) as

$$r = c_r/[g \cos (\phi - \alpha)] = (c_b + gx_r \tan \alpha)/[g \cos(\phi - \alpha)]. \tag{A15}$$

Figure A3 shows an expanded version of the ray path from the source to the bottom.

For a given value of d_s,

$$h_s = d_r + x_r \tan \alpha - d_s. \tag{A16}$$

Also,

$$h_s = r \cos(\phi - \alpha) - r \cos(\gamma + \phi - \alpha)$$

or

$$(\gamma + \phi - \alpha) = \arccos[\cos (\phi - \alpha) - h_s/r] \tag{A17}$$

and

$$x_s = r[\sin(\gamma + \phi - \alpha) - \sin(\phi - \alpha)] \tag{A18}$$

$$x = x_s + x_r. \tag{A19}$$

From Fig. 2 and Eq. (A5),

$$\Delta_s = \arctan[gx_s/(2c_b - gh_s + 2gx_r \tan \alpha], \tag{A20}$$

$$\Delta = \arctan\{gx/[2c_b + gx_r \tan \alpha - g(h_r + h_s)]\}, \tag{A21}$$

$$\theta_s = \Delta_s + \phi - \alpha, \tag{A22}$$

$$\theta = \arctan[(h_s - h_r - x_r \tan \alpha)/x]. \tag{A23}$$

From Eq. (A11), the travel times along the various paths are given by:

Direct path:
$$t_0 = \frac{1}{g} \ln \left| \frac{\cos \theta + \sin \Delta}{\cos \theta - \sin \Delta} \right| \tag{A24}$$

Source to bottom: $\quad t_{sb} = \dfrac{1}{g} \ln \left| \dfrac{\cos \theta_s + \sin \Delta_s}{\cos \theta_s - \sin \Delta_s} \right|$ (A25)

Bottom to receiver: $\quad t_{br} = \dfrac{1}{g} \ln \left| \dfrac{\cos \theta_r + \sin \Delta_r}{\cos \theta_r - \sin \Delta_r} \right|$ (A26)

and the time difference t_d between the direct and the bottom-reflection path is given by

$$t_d = t_{sb} + t_{br} - t_0$$

$$= \frac{1}{g} \ln \left| \frac{\cos \theta_s + \sin \Delta_s}{\cos \theta_s - \sin \Delta_s} \cdot \frac{\cos \theta_r + \sin \Delta_r}{\cos \theta_r - \sin \Delta_r} \cdot \frac{\cos \theta - \sin \Delta}{\cos \theta + \sin \Delta} \right|. \quad \text{(A27)}$$

We now have calculated values of t_d and x for an assigned value of grazing angle for the bottom-reflected signal. Values of t_d computed from Eq. (A27) are shown in Table AI.

Effects of Refraction on Divergence

In a nonrefractive medium, the divergence (or spreading loss) for spherical-wave propagation along a line from r_0 to r is given by

$$D = 20 \log (r/r_0), \quad \text{(A28)}$$

where D is in decibels. When the reflection coefficient for a plane sur-face is measured in such a medium, a correction for the difference between the divergence loss for the direct and that for the reflected signals is necessary if there is a significant difference in the path lengths of the two signals. For the geometries involved in the experiments described in this report, the path lengths of the direct and the reflected signals are virtually the same; however, refractive effects in the medium can produce a significant difference between the divergence of the direct signal and that of the reflected signal. For this reason, the equations developed earlier in this Appendix have been used to calculate this difference in divergence. The procedure was to assume an incremental vertical aperture at the source for the direct signal and, using the equations developed, calculate the spreading loss for the direct signal in the refractive medium. The spreading loss for the reflected signal then was calculated in the same manner. The divergence factor D shown in Table AII was found by taking the difference between the two spreading losses.

Table AI. Time difference between direct and reflected signal arrivals (in milliseconds) as a function of grazing angles; $h_r = 152$ m, $d_r = 3050$ m, $c_b = 1500$ m/s, $g = 0.017$ s^{-1}.

Grazing angle (deg)	α = -5° d_s =			α = 0° d_s =			α = 5° d_s =			α = 10° d_s =		
	500 m	1500 m	2500 m	500 m	1500 m	2500 m	500 m	1500 m	2500 m	500 m	1500 m	2500 m
5	14.0	13.0	9.4	14.5	13.9	12.1	14.8	14.5	13.9	14.8	14.8	14.6
6	17.4	16.3	12.1	18.0	17.3	15.0	18.4	18.1	17.2	18.5	18.4	18.1
7	20.8	19.6	14.9	21.5	20.7	18.0	21.9	21.6	20.4	22.1	21.9	21.6
8	24.3	22.9	17.7	25.0	24.1	20.9	25.5	25.0	23.5	25.6	25.4	24.9
9	27.7	26.2	20.5	28.5	27.5	23.8	28.9	28.4	26.6	29.1	28.8	28.2
10	31.1	29.5	23.3	31.9	30.8	26.7	32.4	31.8	29.6	32.5	32.2	31.4
11	34.5	32.7	26.1	35.3	34.1	29.5	35.8	35.1	32.5	36.0	35.6	34.6
12	37.8	36.0	28.9	38.7	37.4	32.4	39.2	38.4	35.4	39.4	38.9	37.7
13	41.2	39.3	31.7	42.1	40.7	35.2	42.6	41.7	38.3	42.7	42.2	40.7
14	44.5	42.5	34.6	45.4	43.9	38.1	46.0	45.0	41.2	46.1	45.5	43.6
15	47.8	45.7	37.4	48.8	47.1	40.9	49.3	48.2	44.0	49.4	48.7	46.5
16	51.2	48.9	40.2	52.1	50.4	43.7	52.6	51.4	46.9	52.7	52.0	49.4
17	54.4	52.1	43.0	55.4	53.6	46.5	55.9	54.6	49.7	56.0	55.2	52.2
18	57.7	55.3	45.8	58.7	56.8	49.3	59.2	57.8	52.5	59.2	58.3	55.0
19	61.0	58.5	48.6	61.9	60.0	52.2	62.4	61.0	55.3	62.4	61.5	57.8
20	64.2	61.7	51.5	65.2	63.1	55.0	65.7	64.1	58.1	65.6	64.6	60.6

Table AII. Bottom-reflection divergence factor D (in decibels) as a function of grazing angle; h_r = 152 m, d_r = 3050 m, c_b = 1500 m/s, g = 0.017 s^{-1}.

Grazing angle (deg)	α = -5° d_s =			α = 0° d_s =			α = 5° d_s =			α = 10° d_s =		
	500 m	1500 m	2500 m	500 m	1500 m	2500 m	500 m	1500 m	2500 m	500 m	1500 m	2500 m
5	2.76	2.60	1.96	2.76	2.68	2.37	2.80	2.77	2.66	2.80	2.78	2.76
6	2.03	1.93	1.50	2.08	2.02	1.79	2.11	2.08	1.99	2.10	2.09	2.06
7	1.58	1.50	1.20	1.62	1.57	1.40	1.64	1.62	1.54	1.63	1.62	1.60
8	1.26	1.21	0.99	1.30	1.26	1.13	1.31	1.29	1.24	1.30	1.29	1.27
9	1.04	1.00	0.85	1.06	1.04	0.94	1.07	1.06	1.01	1.06	1.05	1.04
10	0.87	0.85	0.74	0.89	0.88	0.81	0.89	0.88	0.85	0.88	0.87	0.86
11	0.75	0.74	0.67	0.76	0.75	0.71	0.76	0.75	0.74	0.74	0.74	0.74
12	0.66	0.65	0.62	0.66	0.66	0.65	0.65	0.66	0.65	0.64	0.64	0.64
13	0.58	0.59	0.59	0.58	0.59	0.60	0.57	0.58	0.59	0.56	0.56	0.58
14	0.53	0.54	0.56	0.52	0.53	0.56	0.51	0.52	0.55	0.50	0.50	0.52
15	0.48	0.50	0.55	0.47	0.49	0.54	0.46	0.48	0.52	0.44	0.45	0.48
16	0.45	0.48	0.55	0.44	0.46	0.53	0.42	0.44	0.50	0.40	0.42	0.46
17	0.42	0.46	0.55	0.41	0.44	0.53	0.39	0.42	0.49	0.37	0.39	0.44
18	0.40	0.44	0.57	0.38	0.42	0.53	0.37	0.40	0.49	0.35	0.36	0.43
19	0.38	0.43	0.58	0.37	0.41	0.54	0.35	0.38	0.49	0.32	0.35	0.43
20	0.37	0.43	0.60	0.35	0.40·	0.56	0.33	0.37	0.50	0.31	0.34	0.43

Appendix B
ESTIMATION OF BOTTOM SEDIMENT PARAMETERS OF THE OCEAN FLOOR
FROM ACOUSTIC REFLECTIVITY MEASUREMENTS

In those cases where Rayleigh reflection exists for the water-sediment interface of the ocean floor, the complex reflection coefficient is given by Eq. (3) of the Introduction. The imaginary part of the sound speed in the sediment is related to the sound attenuation in the sediment as described in that section. When the complex reflection coefficients R_i are known for given grazing angles ϕ_i, Eq. (3) can be reduced to the form

$$\frac{1 - c^2 \cos^2\phi_i}{\rho^2 c^2 \sin^2\phi_i} = \left(\frac{1 - R_i}{1 + R_i}\right)^2 = K_i^2, \tag{B1}$$

or

$$\tan^2\phi_i = \frac{c^2 - 1}{1 - \rho^2 c^2 K_i^2} .$$

If sets of independent measurements exist, then values of the density ρ and the complex sound speed c can be computed from any pair of the measurements by

$$c^2 \text{ (complex)} = 1 + \frac{K_j^2 - K_i^2}{K_j^2 \cot^2\phi_i - K_i^2 \cot^2\phi_j} , \tag{B2}$$

$$\rho^2 \text{ (real)} = \frac{\sin^2\phi_j - \sin^2\phi_i}{K_j^2 \sin^2\phi_j - K_i^2 \sin^2\phi_i} . \tag{B3}$$

41

It follows then that under certain ideal conditions, physical parameters of the sediment such as density, sound speed, and attenuation can be estimated directly from measurements of acoustic reflection from the water-sediment interface.